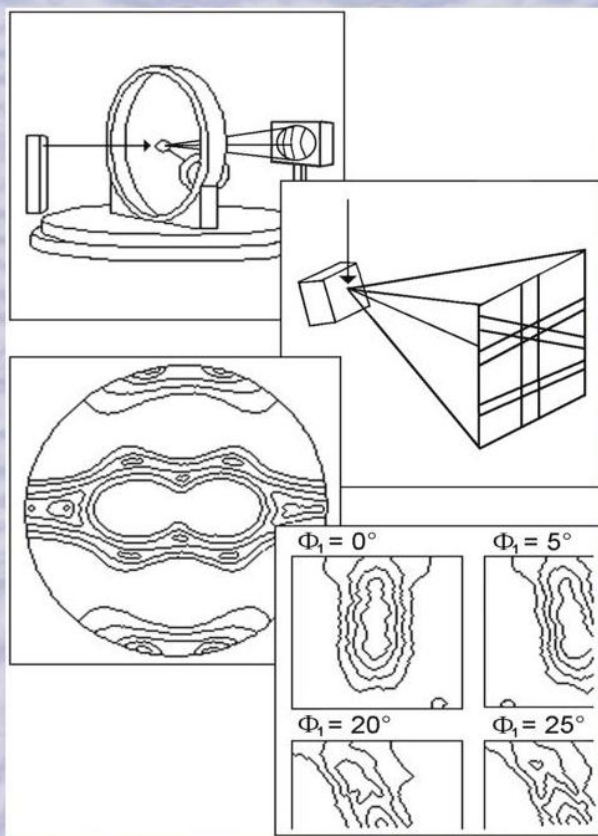# Texture and Anisotropy of Polycrystals III

Edited by
H. Klein and R.A. Schwarzer

Texture and Anisotropy
of Polycrystals III

Texture and Anisotropy of Polycrystals III

Selected, peer reviewed papers from the 3rd International
Conference on Texture and Anisotropy of Polycrystals (ITAP-3)
held in Göttingen, Germany, 23 – 25 September 2009

Edited by

H. Klein and R.A. Schwarzer

International Advisory Committee

Jan Pospiech   (Cracow, Poland)   Honorary Chair
Jan Bonarski   (Cracow, Poland)
Daniel Chateigner   (Caen, France)
Claude Esling   (Metz, France)
David P. Field   (Pullman, USA)
Günter Gottstein   (Aachen, Germany)
Paul van Houtte   (Leuven, Belgium)
Bevis Hutchinson   (Stockholm, Sweden)
Dorte Juul Jensen   (Roskilde, Denmark)
Leo Kestens   (Ghent, Belgium)
Karsten Kunze   (Zürich, Switzerland)
Luca Lutterotti   (Trento, Italy)
Weimin Mao   (Beijing, China)
No-Jin Park   (Gumi, Rep. of Korea)
Yuri A. Perlovich   (Moscow, Russia)
Dave Prior   (Liverpool, UK)
Dierk Raabe   (Düsseldorf, Germany)
Valerie Randle   (Swansea, UK)
Anthony Rollett   (Pittsburgh, USA)
Ashok Kumar Singh   (Hyderabad, India)
Werner Skrotzki   (Dresden, Germany)
Jerzy Szpunar   (Montreal, Canada)
Francis Wagner   (Metz, France)
Klaus Ullemeyer   (Kiel, Germany)
Hasso Weiland   (Alcoa City, USA)

Scientific and Organizing Committee

Helmut Klein   (Univ. Göttingen, Germany)
Bernd Leiss   (Univ. Göttingen, Germany)
Lars Raue   (Univ. Göttingen, Germany)
Jens Walter   (Univ. Göttingen, Germany)
Heinz-Günter Brokmeier   (GKSS and TU Clausthal, Germany)
Robert Schwarzer   (Herrenberg, Germany)
Stefan Zaefferer   (MPIe Düsseldorf, Germany)

Foreword

The Third International Conference on Texture and Anisotropy of Polycrystals, ITAP-3, took place at the Geoscience Center of the University of Göttingen, Germany, on 23 – 25 September 2009, following the intentions and guidelines of ITAP-1 in Clausthal (Germany) 1997 and ITAP-2 in Metz (France) 2004. The purpose of this regional conference was to bring together renowned scientists, researchers, developers, practitioners and students in an informal setting to present and to discuss new and current work.

The conference also hosted four one-day workshops on September 21 and 22. They covered the following topics:
- An Introduction to EBSD and Orientation Microscopy
  by Robert Schwarzer and Stefan Zaefferer
- MAUD workshop: From Diffraction Images to Texture
  by Luca Lutterotti and Daniel Chateigner
- MTEX – Open-Source Software for Texture Analysis
  by Ralf Hielscher and Helmut Schaeben
- Texture Analysis at Large Scale Facilities – Neutron and Synchrotron Radiation
  organized by Hans-Günter Brokmeier.

The conference particularly encouraged the interaction of research students and developing academics with the more established community to foster further cooperation and exchange of ideas. About 100 registered representatives attended the conference. This is all the more remarkable in view of the economic restrictions to which the related industries might have been exposed. The actual economic crisis also cast shadows on the conference in that only a few delegates from industry had got an opportunity to attend.

The great majority of solid-state materials – natural as well as man-made ones – have a poly-crystalline structure that is characterized by the size, shape, arrangement and orientation of the constituting crystals. Crystal orientation is particularly important due to the anisotropy of many physical properties. Therefore, the study of preferred crystal orientations, or crystallographic texture, is of major interest in research and industrial application.
- First of all, texture is one of the fundamental parameters, in addition to crystal structure, lattice defects and element composition, to characterize solid-state materials.
- Texture changes are indicative of solid-state processes of all kind; hence texture can be utilized to advantage in failure analysis as a fingerprint of proper use or misuse of a work-piece.
- Texture enables the geologist to shed light on the processes of rock forming which took place in early days of the history of Earth.
- The knowledge of texture is a prerequisite for all quantitative techniques of materials characterization, which are based on the interpretation of diffraction peak intensities such as the determination of the content of residual austenite in steel, the determination of residual stress by X-ray diffraction, and structure analysis from powder diffraction patterns.
- Most important, however, is texture as the link between anisotropic properties of single crystals and those of polycrystalline material. Its knowledge is utilized in the development and optimization of anisotropic properties of modern structural and functional materials.

Traditionally (crystallographic) texture has referred to the statistical distribution of grain orientations in polycrystals, as obtained from X-ray or neutron pole figure measurement and mathematically described by the Orientation Density Function (ODF). But with the availability of spatially resolving techniques such as Kikuchi diffraction in the SEM and TEM as well as synchrotron diffraction with collimated intense beams, the field of texture research is being increasingly extended to other microstructural features such as grain boundaries, interfaces in general and the 3D characterization of microstructure. This widened experimental view has now again great impact on theory of material science. Texture research is so an appealing field not only for metallurgists, mechanical engineers, materials scientists and geologists, but also for physicists, mathematicians and those working in bioscience.

Noticeable advancements in experimental as well as theoretical methods have been made during the last years. It was the purpose of the third conference in this ITAP series to provide a survey on the state of the art in texture analysis as well as to discuss some typical applications. Eight keynote speakers introduced special themes. 89 contributions were presented in three tracks of parallel sessions and in a poster session. The posters were displayed on all three days.

This proceedings volume contains a selection of 49 peer-reviewed papers being written by authors from 15 countries. They have been arranged in four groups in alphabetic order with respect to the first author. In a few cases the authors preferred to fuse their presentations at the conference in one comprehensive paper. The proceedings volume thus may serve as a guide to this challenging field of science.

Holding a scientific conference is a lot of work. We could not have done it without help from many people. First of all our thanks go to the workshop organizers, all the speakers and those who provided manuscripts for publication in these proceedings. Only by their brainwork and their efforts a scientific conference is enabled to be successful and to lead to fruitful discussions and findings. We also want to give a special thanks to the reviewers.

We would like to thank the members of the International Advisory Committee and the Local Organizing Committee, the colleagues inside and outside Göttingen for their tireless support, as well as the University of Göttingen for providing the conference facilities.

Finally, and most importantly, we would like to thank the conference participants – without your work and participation there would be no conference. We hope your stay in Göttingen was an enjoyable and stimulating one.

Helmut Klein and Robert Schwarzer

Table of Contents

IV. Analysis of Local Texture

I. Keynote Lectures

EBSD-Based Dislocation Microscopy

Brent L. Adams [1a], Calvin J. Gardner [1b] and David T. Fullwood [1c]

[1] Dept. of Mechanical Engineering, Brigham Young University, 435 CTB, Provo, UT 84602 USA

[a] Textura49@gmail.com, [b] strike7dust@gmail.com, [c] dfullwood@byu.edu

Abstract. Recent advances in high-resolution electron backscatter diffraction (EBSD)-based microscopy are applied to the characterization of incompatibility structures near the grain boundaries (GBs) in polycrystals. The principal interest described here is recovery of geometrically-necessary dislocation (density) tensors, of the 2- and 3-D type, described by Nye and Kröner. These developments are presented in the context of the continuum dislocation theory. High resolution data obtained near a single grain boundary in well-annealed, low content steel suggests that it may be possible to measure the intrinsic elastic properties of GBs.

Introduction

This paper describes the application of high-resolution EBSD-based scanning electron microscopy to measure characteristics of dislocation in polycrystalline materials. The simplest possible view is described here – that of single-phase polycrystals, where the main defect structures are dislocations, within and between the constituent crystallites, and within the grain boundaries that separate the grains of the material. That which is observable about these defects is the (elastic) self-stresses that preserve the compatibility of the displacement field. It will be shown that these distortions of the crystal lattice can be recovered from the EBSD patterns.

The notion that incompatible plastic strains must be coupled with compensating elastic strains in order to maintain compatibility, reaches back at least to the foundational work of Eshelby [1] in 1957, where these incompatible strains were referred to as stress-free transformation strains in treating ellipsoidal inclusion problems. Earlier, in 1953, Nye had presented a geometrical theory of dislocation in crystals [2]; that workwas extended to include consideration of elastic self-stresses in the masterwork of Kröner in 1958 [3]. A significant retrospective of that work, written by Kröner himself, was published in 2001 [4]. Much of the focus of this paper will be with Kröner's work in mind; and to the extent possible his notation will be maintained here. For readers desiring a systematic, detailed presentation of the continuum theory of dislocations, the monographs of Teodosiu [5] and Mura [6] are recommended.

Connecting these theoretical constructs to experimental measurements is most direct with EBSD. The first observations of backscattered diffraction patterns were reported by Nishikawa and Kikuchi in 1928 [7]. These images were recorded on film. The first detailed description of the physics of backscattering was detailed in the work paper of Alam, Blackman and Pashley in 1953 [8]. Venables [9] seems to have been the first to employ a camera located in the chamber of the electron microscope for recording these EBSD patterns. Automated scanning and real-time analysis of EBSD-patterns, to form crystallographically-specific images, was reported by Adams and co-workers in 1993 [10]. The acronym OIM, which stands for orientation imaging microscopy, has been used to describe 2-D images of microstructure, where the constituent features are discriminated by lattice orientation. Numerous refinements and applications of OIM and EBSD-related microscopy have been detailed in the monographs edited by Schartz and co-workers in 2000 [11] and 2009 [12].

Using conventional OIM capabilities, Sun *et al.* [13] made the first measurements of Nye's dislocation density tensor – in an Al bicrystal. The resolution of the conventional EBSD

techniques, based upon the Hough transformation for indexing lattice orientation, has been addressed by El-Dasher et al. [14], and Field [15], and more recently by Kacher and Adams [16]. The Hough-based methods achieve a limiting angular resolution of ~0.5°, which restricts their application to materials with high dislocation densities ($>10^{15}$ m^{-2}). Of particular interest here, however, are the high-resolution cross-correlation-based techniques pioneered by Troost and co-workers in 1993 [17], and more completely developed by Wilkinson et al. in 2006 [18]. An augmentation of Wilkinson's approach, named the simulated-pattern method (SPM), was introduced by Kacher et al. in 2009 [19]. This paper describes applications of the Wilkinson method, using elements of the SPM augmentation to precisely locate the EBSD pattern center, to the characterization of dislocation tensor fields. Due to space limitations, it will not describe the higher-order spatial correlation functions of the dislocation tensor field; if the reader is interested in these ideas, he is referred to the work of Landon et al. [20]. For the same reasons, a detailed description of pattern center location will not be described.

Basic relations of continuum dislocation theory

Our purpose for this section of the paper is to describe the context for the experimental measurements. Microstructure representation, with its varied and multiplied possibilities, must be guided by physical theory to settle its context. The authors contend that localization relations present a compelling context for EBSD-based microscopy, and vice-versa. It is illustrated that the details of the local stress condition are dependent upon the local elastic polarization, and upon the field of dislocation, contained in both the grain interiors and the grain boundaries.

Let ε_{ij} represent the total strain in the material, e_{ij} represents the elastic strain, and ε_{ij}^* represents the 'eigenstrain' (the terminology of Mura [6]) caused by the presence of dislocations in the sample. Then

$$\varepsilon_{ij} = e_{ij} + \varepsilon_{ij}^*. \tag{1}$$

And the compatibility relation may be written:

$$\varepsilon_{ij} = \frac{1}{2}\left(u_{i,j} + u_{j,i}\right) \tag{2}$$

in terms of the displacement components u_i and their spatial derivatives, as denoted by $u_{i,j}$. We also have the elastic constitutive relations:

$$\sigma_{ij} = C_{ijkl}e_{kl} = C_{ijkl}\left(\varepsilon_{kl} - \varepsilon_{kl}^*\right). \tag{3}$$

It suits our purposes here to write the local stiffness tensor in terms of a perturbation from a reference stiffness tensor:

$$C_{ijkl}(\mathbf{x}) = C_{ijkl}^r + C_{ijkl}'(\mathbf{x}). \tag{4}$$

In the absence of external body forces, the equilibrium condition $\sigma_{ij,j} = 0$ may be combined with the previous two equations to give:

$$\left[\left(C_{ijkl}^r + C_{ijkl}'(\mathbf{x})\right)\left(\varepsilon_{kl}(\mathbf{x}) - \varepsilon_{kl}^*(\mathbf{x})\right)\right]_{,j} = 0$$
$$C_{ijkl}^r \varepsilon_{kl,j}(\mathbf{x}) + \left[C_{ijkl}'(\mathbf{x})\varepsilon_{kl}(\mathbf{x}) - \left(C_{ijkl}^r + C_{ijkl}'(\mathbf{x})\right)\varepsilon_{kl}^*(\mathbf{x})\right]_{,j} = 0 \tag{5}$$

From the symmetry of C_{ijkl}^r we may write $C_{ijkl}^r \varepsilon_{kl,j} = C_{ijkl}^r u_{k,lj}$, and combining the second term into a fictitious body force:

$$F_i(\mathbf{x}) = \left[C_{ijkl}'(\mathbf{x}) \varepsilon_{kl}(\mathbf{x}) - \left(C_{ijkl}^r + C_{ijkl}'(\mathbf{x}) \right) \varepsilon_{kl}^*(\mathbf{x}) \right]_{,j}. \tag{6}$$

Thereby we arrive at the fundamental differential equation that we wish to solve:

$$C_{ijkl}^r u_{k,lj} + F_i = 0. \tag{7}$$

Define a Green's function, G, such that:

$$C_{ijkl}^r G_{km,lj}(\mathbf{x} - \mathbf{x}') + \delta(\mathbf{x} - \mathbf{x}') \, \delta_{im} = 0. \tag{8}$$

Now multiply Eq. 7 by G, and integrate. Using integration by parts twice on the first term to obtain second derivatives of G, and then using Eq. 8:

$$u_k(\mathbf{x}) = \int_V G_{ki}(\mathbf{x} - \mathbf{x}') F_i(\mathbf{x}') \, d\mathbf{x}'. \tag{9}$$

Hence

$$
\begin{aligned}
\varepsilon_{kl}(\mathbf{x}) &= \int_V \frac{1}{2} \left(G_{ki,l}(\mathbf{x} - \mathbf{x}') + G_{li,k}(\mathbf{x} - \mathbf{x}') \right) F_i(\mathbf{x}') \, d\mathbf{x}' \\
&= \int_V \frac{1}{2} \left(G_{ki,l}(\mathbf{x} - \mathbf{x}') + G_{li,k}(\mathbf{x} - \mathbf{x}') \right) \left[C_{ijmn}'(\mathbf{x}') \varepsilon_{mn}(\mathbf{x}') - \left(C_{ijmn}^r + C_{ijmn}'(\mathbf{x}') \right) \varepsilon_{mn}^*(\mathbf{x}') \right]_{,j} d\mathbf{x}'
\end{aligned} \tag{10}
$$

Using Eq. 1 this becomes:

$$\varepsilon_{kl}(\mathbf{x}) = \int_V \frac{1}{2} \left(G_{ki,l}(\mathbf{x} - \mathbf{x}') + G_{li,k}(\mathbf{x} - \mathbf{x}') \right) \left[C_{ijmn}'(\mathbf{x}') e_{mn}(\mathbf{x}') - C_{ijmn}^r \varepsilon_{mn}^*(\mathbf{x}') \right]_{,j} d\mathbf{x}'. \tag{11}$$

To deal with the singularity in the Green's function at $\mathbf{x} = \mathbf{x}'$ we integrate by parts between a sphere about the singularity and an infinite sphere (see Torquato [21]):

$$
\begin{aligned}
\varepsilon_{kl}(\mathbf{x}) &= \left[\int_S \frac{1}{2} \left(G_{ki,l}(\mathbf{x} - \mathbf{x}') + G_{li,k}(\mathbf{x} - \mathbf{x}') \right) \left[C_{ijmn}'(\mathbf{x}') e_{mn}(\mathbf{x}') - C_{ijmn}^r \varepsilon_{mn}^*(\mathbf{x}') \right] n_j \, dS \right]_{\substack{sphere\,with\\ \mathbf{x}' \to x}}^{\substack{sphere\,with\\ \mathbf{x}' \to \infty}} \\
&- \int_{V'} \frac{1}{2} \left(G_{ki,lj}(\mathbf{x} - \mathbf{x}') + G_{li,kj}(\mathbf{x} - \mathbf{x}') \right) \left[C_{ijmn}'(\mathbf{x}') e_{mn}(\mathbf{x}') - C_{ijmn}^r \varepsilon_{mn}^*(\mathbf{x}') \right] d\mathbf{x}'
\end{aligned} \tag{12}
$$

The volume integral may be compared with Mura [6] Eq. 6.1 for the case that C is constant.
Ignore the eigenstrain surface integrals for now; let them be combined in the tensor, $\mathbf{S}(\mathbf{x})$. Consider the value of the elastic surface integrals. For the integral on the infinitesimal sphere $\mathbf{x}' \to \mathbf{x}$ one may assume that the local stiffness and strain are approximately constant, and can be moved outside of the integral sign. Then for an isotropic reference tensor we may write [22, 23],

$$E_{ijkl} = \int\limits_{S:x^*\to x} \frac{1}{2}\left(G_{ki,l}(\mathbf{x}-\mathbf{x'}) + G_{li,k}(\mathbf{x}-\mathbf{x'})\right) n_j dS$$

$$= \frac{1}{15\mu}\left\{\frac{\lambda+\mu}{\lambda+2\mu}\delta_{ij}\delta_{kl} - \frac{3\lambda+8\mu}{\lambda+2\mu}I_{ijkl}\right\} . \tag{13}$$

The integral on the infinite sphere may be approximated as [24]:

$$I^\infty \approx \mathbf{E}\overline{\mathbf{C}'}\mathbf{e}^\infty , \tag{14}$$

where $\mathbf{e}^\infty$ is the applied strain at infinity. Hence we may rewrite the elastic surface integrals as:

$$\left[\int\limits_S \frac{1}{2}\left(G_{ki,l}(\mathbf{x}-\mathbf{x'}) + G_{li,k}(\mathbf{x}-\mathbf{x'})\right)C'_{ijmn}(\mathbf{x'})e_{mn}(\mathbf{x'})n_j dS\right]_{\substack{sphere with\\ \mathbf{x'}\to x}}^{\substack{sphere with\\ \mathbf{x'}\to\infty}} \approx \mathbf{E}\overline{\mathbf{C}}\mathbf{e}^\infty - \mathbf{E}\mathbf{C'}(\mathbf{x})\mathbf{e}(\mathbf{x}) \tag{15}$$

Clearly, if $\mathbf{C}^R = \overline{\mathbf{C}}$ (the over-bar signifying the volume average) then $\overline{\mathbf{C'}} = \mathbf{0}$, and I^∞, as calculated from Eq. (14), tends to zero. Using the usual notation [23, 24]:

$$\Phi(\mathbf{x}-\mathbf{x'}) = \frac{1}{2}\left(G_{ki,lj}(\mathbf{x}-\mathbf{x'}) + G_{li,kj}(\mathbf{x}-\mathbf{x'})\right) , \tag{16}$$

we may write

$$\begin{aligned}
\sigma(\mathbf{x}) &= \mathbf{C}(\mathbf{x})\mathbf{e}(\mathbf{x}) = \mathbf{C}(\mathbf{x})\left(\varepsilon(\mathbf{x}) - \varepsilon^*(\mathbf{x})\right)\\
&= \mathbf{C}(\mathbf{x})\mathbf{E}\overline{\mathbf{C'}}(\mathbf{x})\mathbf{e}^\infty - \mathbf{C}(\mathbf{x})\mathbf{E}\mathbf{C'}(\mathbf{x})\mathbf{e}(\mathbf{x}) - \mathbf{C}(\mathbf{x})\mathbf{S}(\mathbf{x})\\
&\quad - \mathbf{C}(\mathbf{x})\int\limits_{V'}\Phi(\mathbf{x}-\mathbf{x'})\left[\mathbf{C'}(\mathbf{x'})\mathbf{e}(\mathbf{x'}) - \mathbf{C}^r\varepsilon^*(\mathbf{x'})\right]d\mathbf{x'} - \mathbf{C}(\mathbf{x})\varepsilon^*
\end{aligned} \tag{17}$$

From Mura [6] Eqs. 6.1 and 37.13, when the eigenstrain is due purely to dislocations:

$$\begin{aligned}
&- C_{pqkl}\int\limits_V \frac{1}{2}\left(G_{ki,lj}(\mathbf{x}-\mathbf{x}^*) + G_{li,kj}(\mathbf{x}-\mathbf{x}^*)\right)C_{ijmn}\varepsilon_{mn}^*(\mathbf{x}^*)d\mathbf{x}^* - C_{pqkl}\varepsilon_{kl}^*(\mathbf{x})\\
&= C_{pqkl}\int\limits_V \in_{lnh} G_{ki,j}(\mathbf{x}-\mathbf{x}^*)C_{ijmn}\alpha_{hm}(\mathbf{x}^*)d\mathbf{x}^*
\end{aligned} \tag{18}$$

Hence:

$$\begin{aligned}
\sigma_{pq}(\mathbf{x}) &= C_{pqkl}(\mathbf{x})E_{klmn}\left(\overline{C'_{mnrs}}e_{rs}^\infty - C'_{mnrs}(\mathbf{x})e_{rs}(\mathbf{x})\right)\ldots\\
&\quad + C_{pqkl}(\mathbf{x})\int\limits_{V'}\in_{lnh} G_{ki,j}(\mathbf{x}-\mathbf{x'})C_{ijmn}^r\alpha_{hm}(\mathbf{x'})d\mathbf{x'} - C_{pqkl}(\mathbf{x})\int\limits_{V'}\Phi_{klij}C'_{ijmn}(\mathbf{x'})e_{mn}(\mathbf{x'})d\mathbf{x'}
\end{aligned} \tag{19}$$

The right hand side of Eq. (18) could be reached directly from the eigenstrain component of Eq. (11); hence we can deal with the singularity relating to the eigenstrain term (temporarily referred to as $\mathbf{S}(\mathbf{x})$ above) by integrating Eq. (18) by parts:

$$\int_{V'} \in_{\text{lnh}} G_{ki,j}(\mathbf{x}-\mathbf{x}')C^r_{ijmn}\alpha_{hm}(\mathbf{x}')d\mathbf{x}' = \left[\int_{S}\in_{\text{lnh}} G_{ki}(\mathbf{x}-\mathbf{x}')C^r_{ijmn}\alpha_{hm}(\mathbf{x}')\mathbf{n}_j ds\right]^{\substack{sphere \\ \mathbf{x}'\to\infty \\ sphere \\ \mathbf{x}'\to\mathbf{x}}}$$
$$-\int_{V'}\in_{\text{lnh}} G_{ki}(\mathbf{x}-\mathbf{x}')C^r_{ijmn}\alpha_{hm,j}(\mathbf{x}')d\mathbf{x}' \tag{20}$$

We treat two surface integrals as for the elastic case (Eq. (15)), with an approximate value for the infinite sphere. Let

$$S_{ijk}(\mathbf{x}-\mathbf{x}') = \int_{S:\mathbf{x}'\to\mathbf{x}} G_{ki}(\mathbf{x}-\mathbf{x}')\,\mathbf{n}_j ds \tag{21}$$

Then

$$\left[\in_{\text{lnh}} G_{ki}(\mathbf{x}-\mathbf{x}')C^r_{ijmn}\alpha_{hm}(\mathbf{x}')\mathbf{n}_j ds\right]^{\substack{sphere \\ \mathbf{x}'\to\infty \\ sphere \\ \mathbf{x}'\to\mathbf{x}}} \approx \in_{\text{lnh}} S_{ijk}C^r_{ijmn}\left(\alpha^\infty_{hm}-\alpha_{hm}(\mathbf{x})\right) \tag{22}$$

Then:

$$\sigma_{pq}(\mathbf{x}) = C_{pqkl}(\mathbf{x})E_{klmn}\left(\overline{C'_{mnrs}}e^\infty_{rs} - C'_{mnrs}(\mathbf{x})e_{rs}(\mathbf{x})\right) - C_{pqkl}(\mathbf{x})\in_{\text{lnh}} S_{ijk}C^r_{ijmn}\left(\alpha^\infty_{hm}-\alpha_{hm}(\mathbf{x})\right)$$
$$+ C_{pqkl}(\mathbf{x})\int_{V'}\in_{\text{lnh}} G_{ki}(\mathbf{x}-\mathbf{x}')C^r_{ijmn}\alpha_{hm,j}(\mathbf{x}')d\mathbf{x}' - C_{pqkl}(\mathbf{x})\int_{V'}\Phi_{klij}\,C'_{ijmn}(\mathbf{x}')e_{mn}(\mathbf{x}')d\mathbf{x}' \tag{23}$$

Although quite complex in the form of its various terms, relation (23) defines the familiar dependence of local stress at position **x** upon the detailed spatial placement of lattice orientation at **x'**, through terms such as the elastic stiffness tensor, or its polarization. Less familiar is its dependence upon the placement of dislocation, throughout the body. (The reader is reminded that the dislocation tensor is related to the curl of the elastic distortion tensor, β, where $\beta_{ij} = \partial u^e_j / \partial x_i$ are spatial derivatives of the elastic displacement field. Fundamental to these developments is the idea that compatibility of the total displacement field requires that

$$\alpha = curl\,\beta^e = -curl\,\beta^p \tag{24}$$

It is this fundamental curl-free condition that enables the high-resolution EBSD-based experimental measurements to be connected to the constructs of the continuum dislocation theory of Kröner[4].)

Measurements in Low Content Steel

A sample of low-content steel, annealed to achieve a nominally columnar grain morphology, with grain size of ~ 500 μm, was sectioned, polished and examined within a 2x2 μm region using an FEI-Philips XL-30 SFEG scanning electron microscope. EBSD images were captured using a DigiView CCD camera supplied by TSL-EDAX at full resolution (without binning). These images were obtained over a square grid of points at 20 nm step size over the complete region, and stored for subsequent processing off-line. A region was selected containing a single grain boundary oriented nominally in a plane parallel to that defined by the beam direction and the sample normal. Given the columnar nature of the grain morphology, this geometry gives the best possible spatial resolution (i.e. the minimum volume of grain boundary region contained in the electron beam interaction volume), assuming that the grain boundary normal is perpendicular to this plane.

At several points taken near the centroids of the two grains, reference EBSD patterns were taken. These reference images were used for pattern center calibration, and to provide nominally strain free reference patterns from which Fast Fourier Transform (FFT) algorithms were applied to

recover estimates of the local elastic distortion tensor using Wilkinson's equations [18]. Initial estimates of lattice orientation were then corrected using the recovered off-diagonal components of the elastic distortion tensor. Figure 1 depicts the principal measurements obtained through a false-color image. The elastic disturbance of the grain boundary region is evident in this image, as well as a horizontal region of disturbance extending across the boundary.
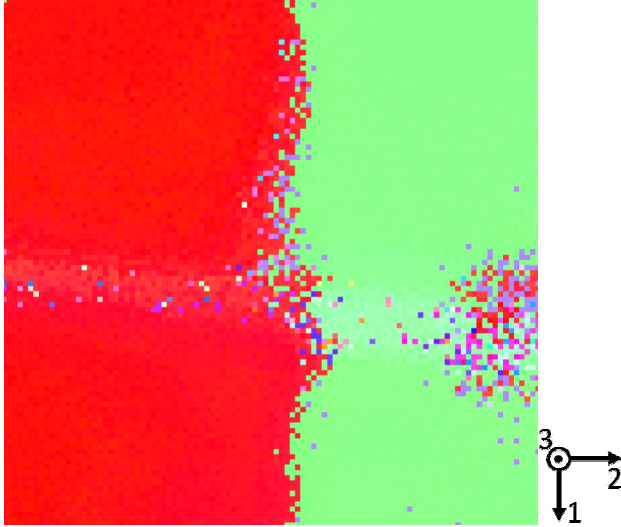
Figure 1. False color image of the recovered lattice orientation near the studied grain boundary.

Figure 2 depicts the sum of the magnitudes of the six available components of the lattice curvature tensor. The very small magnitude of these curvatures is notable. Figure 3 shows the summed magnitude of the three measurable components of the dislocation density tensor, plotted as a field. Related to the coordinate frame shown in Fig. 1, the available components are α_{31}, α_{32}, and α_{33}. These measurements include the elastic strain gradient contributions introduced by Kröner[4], but not included in Nye's treatment [2]. The units shown, in m^{-1}, can be related to the more conventional units of dislocation density, m^{-2}, by dividing the field values by the length of the Burger's vector in Fe, which is ~ 0.25 nm. And, lastly, Fig. 4 depicts the sum over the magnitudes of the 6 components of the surface dislocation density tensor. It is presumed, in forming these values that the interface normal lies in the 2-direction, as defined in Fig. 1. Thus, the magnitudes of $\alpha_{11}^{s}, \alpha_{12}^{s}, \alpha_{13}^{s}, \alpha_{31}^{s}, \alpha_{32}^{s}, \alpha_{33}^{s}$ are accessible. Note that the spiked feature near the center of the plot associates with the horizontal feature in the data set.
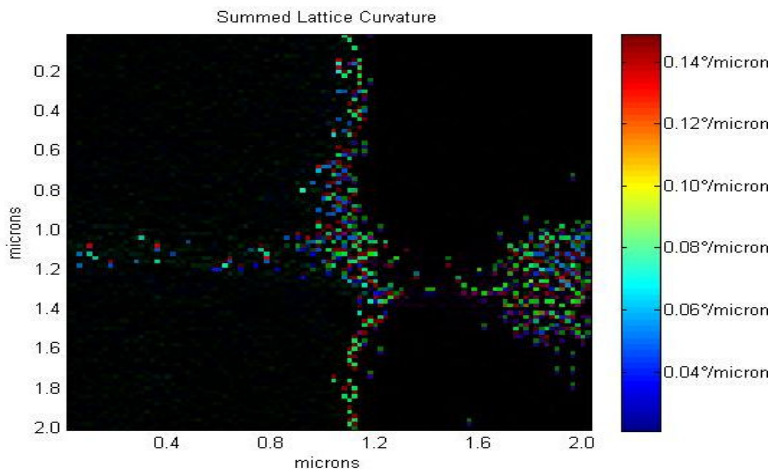
Figure 2. Summation over the magnitudes of the six available components of the lattice curvature tensor, in units of degrees/micron.
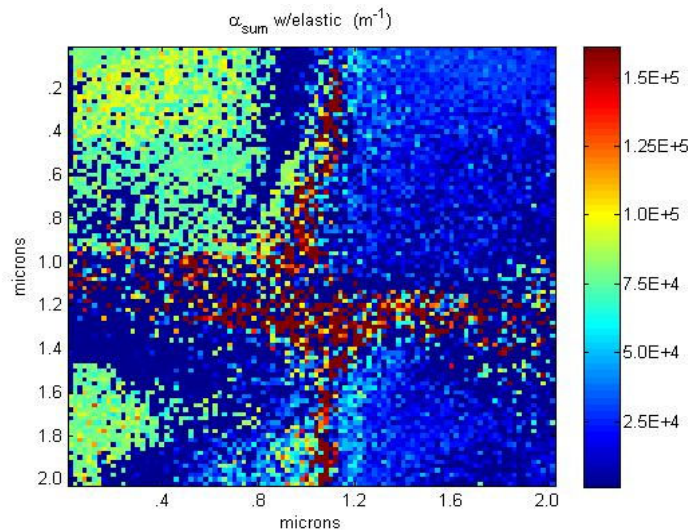
Figure 3. Summation of the magnitudes of the three directly measurable components of the dislocation tensor (including the elastic strain gradient contributions).
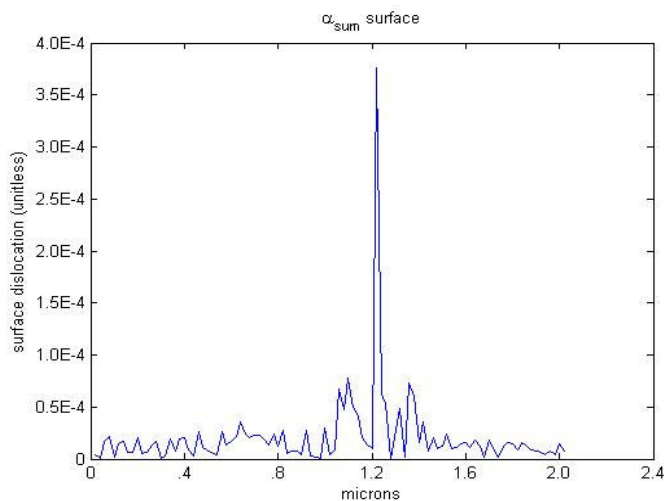
Figure 4. Summation over the magnitudes of the six components of the surface dislocation density tensor along the vertical grain boundary.

Summary and Conclusions

Elastic continuum theory, based upon solutions to the stress equilibrium equations and considerations of compatibility, clearly identify two sources of influence upon stress localization in single phasepolycrystals: the spatial heterogeneity of the elastic stiffness present within the grain structure, and the presence of dislocation within grain interiors and at grain boundaries. Experimental capability for recovering the first of these effects is now routine, through EBSD-based microscopy of ordinary resolution. In this paper we have asked the question as to whether the second of these influences, coming from the presence of dislocation, can be recovered by high-resolution EBSD methods. Although the results presented in Figs. 1-4 are preliminary, they suggest that the intrinsic dislocation structure associated with elastic disturbances near grain boundaries (arising because of local disturbances in the atomic structure) may in fact be accessible via EBSD.

If these capabilities can be satisfactorily developed and exploited, it may be possible to map the elastic (and yield) properties of individual grain boundaries back to their five degrees of crystallographic freedom. Such a mapping could have profound significance in extending theory for microstructure design to the design of grain boundary character and distribution, for the purpose of mitigating extreme value properties, such as fracture and fatigue, where it is known that properties depend upon the peaks within the stress field.

References

[1] J.D. Eshelby: The determination of the elastic field of an ellipsoidal inclusion, and related problems. Proc. Royal Soc. London A Vol. 241 (1957), p. 376.

[2] J.F. Nye: Some geometrical relations in dislocated crystals. Acta Metallurgica Vol. 1 (1953), p. 153.

[3] E. Kröner: Continuum theory of dislocations and self-stresses. Ergebnisse der Angewandten Mathematik Vol. 5 (1958), p. 1327.

[4] E. Kröner: Benefits and shortcomings of the continuous theory of dislocations. Int. J. Solids and Struct. Vol. 38 (2001), p. 1115.

[5] C. Teodosiu: *Elastic Models of Crystal Defects*. Springer-Verlag, Berlin (1982).

[6] T. Mura: *Micromechanics of Defects in Solids*. Martinus Nijhoff Publishers, Boston (1987).

[7] S. Nishikawa and S. Kikuchi: The diffraction of cathode rays by calcite. Proc. Imperial Acad. (Japan) Vol. 4 (1928), p. 475.

[8] M.N. Alam, M. Blackman and D.W. Pashley: High-angle Kikuchi patterns. Proc. Royal Soc. London A Vol. 221 (1954), p. 224.

[9] J.A. Venables and C.J. Harland: Electron back-scattering patterns - A new technique for obtaining crystallographic information in the scanning electron microscope. Phil. Mag. Vol. 27 (1973), p. 1193.

[10] B.L. Adams, S.J. Wright and K. Kunze: Orientation imaging: The emergence of a new microscopy. Metallurgical Transactions A (Physical Metallurgy and Materials Science) Vol. 24A (1993), p. 819.

[11] A.J. Schwartz, M. Kumar and B.L. Adams (editors): *Electron Backscatter Diffraction in Materials Science*. Kluwer Academic / Plenum Publishers, New York (2000).

[12] A.J. Schwartz, M. Kumar, B.L. Adams and D.P. Field (editors): *Electron Backscatter Diffraction in Materials Science*, 2nd Edition. Springer, New York (2009).

[13] S. Sun, B.L. Adams and W.E. King: Observations of lattice curvature near the interface of a deformed aluminium bicrystal. Phil. Mag. A: Physics of Condensed Matter, Structure, Defects and Mechanical Properties Vol 80 (2000), p. 9.

[14] B.S. El-Dasher, B.L. Adams and A.D. Rollett: Viewpoint: Experimental recovery of geometrically necessary dislocation density in polycrystals. Scripta Materialia Vol. 48 (2003), p. 141.

[15] D. Field: Recent advances in the application of orientation imaging. Ultramicroscopy Vol. 67 (1997), p. 1.

[16] J. Kacher and B.L. Adams: Resolution considerations for EBSD-based dislocation density estimates. Scripta Materialia   *Submitted 2009*.

[17] K.Z. Troost, P. Van der Sluis and D.J. Gravesteijn: Microscale elastic-strain determination by backscatter Kikuchi diffraction in the scanning electron microscope. Appl. Phys. Lett. Vol. 62 (1993), p. 1110.

[18] A.J. Wilkinson, G. Meaden and D.J. Dingley: High-resolution elastic strain measurement from electron backscatter diffraction patterns: New levels of sensitivity. Ultramicroscopy Vol. 106 (2006), p. 307.

[19] J. Kacher, C. Landon, B.L. Adams and D. Fullwood: Bragg's law diffraction simulations for electron backscatter diffraction analysis. Ultramicroscopy Vol. 109 (2009), p. 1148.

[20] C.D. Landon, B. Adams and J. Kacher: High resolution methods for characterizing mesoscale dislocation structures. J. Eng. Mater. Technol. Vol. 130 (2008), p. 021004-1

[21] S. Torquato: Effective stiffness tensor of composite media. I. Exact series expansions. J. Mech. Phys. Solids Vol. 45 (1997), p. 1421.

[22] S. Torquato: *Random Heterogeneous Materials*. Springer-Verlag, New York (2002).

[23] E. Kröner: Statistical modelling. In: J. Gittus and J. Zarka (editors): *Modeling Small Deformation in Polycrystals*. Elsevier, (1986).

[24] D.T. Fullwood, S.R. Kalidindi, B.L. Adams and S. Ahmadi: A discrete Fourier transform framework for localization relations. Computers, Materials and Continua Vol. 299 (2009), p. 1.

Calculation methods to determine crystallographic elements: interface plane, surfaces plane and twinning elements, based on electron diffraction orientation measurements by SEM and TEM

Claude Esling[1, a], Yudong Zhang[1, a], Jacques Muller[1, a], Xiang Zhao[2, b], and Liang Zuo[2, b]

[1]LETAM, CNRS FRE 3143 (Former UMR 7078), University of Metz, F-57045 Metz, France
[2] School of Materials and Metallurgy, Northeastern University, 110004 Shenyang, China

[a]yudong.zhang@univ-metz.fr; [b]claude.esling@univ-metz.fr; [c]jacques.muller@univ-metz.fr, [d]zhaox@ mail.neu.edu.cn, [d]lzuo@ mail.neu.edu.cn

Abstract: In the present work, we summarize three calculation methods to determine some specific crystallographic elements based on electron diffraction orientation measurements by SEM and TEM. The first one is to determine the plane indices of the faceted interfaces where the orientation relationships (ORs) between the adjacent crystals are reproducible. To acquire the orientation data, we need to prepare only one sample surface but not two perpendicular sample surfaces as usually required in the standard double trace method. The second is to characterize the surface crystalline planes and directions of a faceted nano-particle under TEM imaging and diffraction mode. With the determination of the edge trace vectors and then the plane normal vectors in the screen coordinate system of TEM, their Miller indices in the crystal coordinate system can be calculated through coordinate transformation. The third method is to determine the twin type and the twinning elements based on the orientation information acquired by SEM EBSD measurements from the two twinned crystals through misorientation calculations. These methods will facilitate related studies.

Introduction

With the advent of electron diffraction orientation determination realized in SEM [1] and TEM [2, 3], microstructural analyses have gone one step further towards the quantitative level with the individual orientation information of the materials. The related studies on texture, on crystallographic plane of interfaces and on crystallographic characteristics of twinning, as commonly encountered in microstructural examinations, have become precise and easy by the availability of the direction orientation information through electron diffraction pattern acquiring and indexing system attached to either SEM or TEM. To further facilitate the related studies, the determination methods are needed. Based on such practical requirements, we have devoted to working out the possible calculation methods. The methods to determine the crystallographic reproducible faceted interface plane [4], that to determine the surface plane of nano-particles [5] and that to determine the twin type and twinning elements [6] based on the orientation data obtained by SEM or TEM are summarized in this work.

Indirect two trace method to determine the crystallographic plane of specific interfaces

Many solid-state phase transformations bring about crystallographically correlated phases with faceted low energy interfaces, like twin boundaries, martensitic variant boundaries and habit planes between precipitates and matrix. In most cases the orientation relationships (ORs) at interfaces are frequently reproducible and the interfaces are of the same crystallographic nature. Indexing their crystalline plane has involved constant effort. So far, the two-trace method [7] has long been accepted and widely practiced in experimentally determining the interface planes in various phase

systems. However, this method suffers some drawbacks. For instance, it requires great care in sample preparations and tedious efforts in measurements. To make such measurements easily applicable and accurate, we propose an indirect two-trace method, as described below.

We refer the basic principle of the indirect two-trace method to that of the traditional two-trace method. It is essential to find out two independent traces that belong to two interfaces of the same type on one sample surface. The vector product of the two trace vectors in a Cartesian crystal coordinate system then defines the normal of the interface plane. In contrast to the two-trace method, it requires no more preparation of two perpendicular sample surfaces. This is because the two trace vectors are obtained from two macroscopically differently oriented but crystallographically identical interface planes that are visible on the same sample surface, instead of from exactly one interface plane but on two different sample surfaces.

Consider that two interfaces 1 and 2 – at which the phases α and β meet – intersect with a sample surface, as schematically shown in Fig. 1. The crystal orientations of the concerned α and β phases adjacent to the interfaces 1 and 2 are denoted as $_1g^{\alpha}$, $_1g^{\beta}$, $_2g^{\alpha}$ and $_2g^{\beta}$, respectively. They can be determined from their SEM electron back-scattering patterns or the TEM Kikuchi patterns. We suppose that the two interfaces are crystallographically identical, *i.e.* with the same misorientation Δg and the same interface plane normal in a fixed orthonormal crystal coordinate system K^{α} (or K^{β}), but differently oriented with respect to the orthonormal sample coordinate system K^{S}. The traces of the interfaces on the sample surface are then specified by the normalized unit vectors $_1\vec{V}$ and $_2\vec{V}$ in the sample coordinate system K^{S}. Their equivalent vectors, expressed in the K^{α} (or K^{β}), are obtained through the following coordinate system transformations using the orientations $_1g^{\alpha}$ (or $_1g^{\beta}$) and $_2g^{\alpha}$ (or $_2g^{\beta}$) in matrix notation,

$$
\begin{aligned}
_1\vec{V}_j^{K^{\alpha}} &= (S_j^{\alpha})^{-1}(_1g^{\alpha})^{-1}\,_1\vec{V} \\
_2\vec{V}_j^{K^{\alpha}} &= (S_j^{\alpha})^{-1}(_2g^{\alpha})^{-1}\,_2\vec{V}
\end{aligned}
\quad (j=1,2,3,\ldots,J) \quad \text{or} \quad
\begin{aligned}
_1\vec{V}_k^{K^{\beta}} &= (S_k^{\beta})^{-1}(_1g^{\beta})^{-1}\,_1\vec{V} \\
_2\vec{V}_k^{K^{\beta}} &= (S_k^{\beta})^{-1}(_2g^{\beta})^{-1}\,_2\vec{V}
\end{aligned}
\quad (k=1,2,3,\ldots,K) \quad (1)
$$

where S_j^{α} (or S_k^{β}) are the jth (or k[th]) rotational elements of the crystal symmetry group of the α (or β) phase. Owing to the crystal symmetries, one and the same macroscopic trace vector is represented – in the general case – by J number of crystallographic equivalents in the α crystal system and K number in the β crystal system. As the two interfaces are supposed to be of the same type, the two trace vectors – when transformed into the K^{α} (or K^{β}) crystal system – must be in the same plane. The normal $\vec{n}$ to the interface plane in the either K^{α} or K^{β} is given by

$$
\vec{n}_{j''}^{K^{\alpha}} = {_1\vec{V}_j^{K^{\alpha}}} \times {_2\vec{V}_{j'}^{K^{\alpha}}} \quad \text{or} \quad \vec{n}_{k''}^{K^{\beta}} = {_1\vec{V}_k^{K^{\beta}}} \times {_2\vec{V}_{k'}^{K^{\beta}}}
\tag{2}
$$

where $_1\vec{V}_{j''}^{K^{\alpha}}$ (or $_2\vec{V}_{j''}^{K^{\alpha}}$) are the j''th (or j'''th) equivalents of the $_1\vec{V}$ (or $_2\vec{V}$) in the K^{α}, and $_1\vec{V}_{k''}^{K^{\beta}}$ (or $_2\vec{V}_{k''}^{K^{\beta}}$) are the k''th (or k'''th) equivalents of the $_1\vec{V}$ (or $_2\vec{V}$) in the K^{β}, respectively. The interface plane in the K^{α} (or K^{β}) can thus be determined. The only concern of this method is how to pick out the correct unique solution after the multiplication induced by crystal symmetry. We solved this problem by using the following condition. Considering that the two interfaces provide the same misorientation between the α and β phases, *i.e.* $_1\Delta g \equiv {_2\Delta g}$, the following relation can be used to locate the symmetry elements that produce the correct unique solution.

$$(S_k^{\beta})^{-1} \cdot ({}_1 g^{\beta})^{-1} \cdot ({}_1 g^{\alpha}) \cdot (S_j^{\alpha}) = (S_{k'}^{\beta})^{-1} \cdot ({}_2 g^{\beta})^{-1} \cdot ({}_2 g^{\alpha}) \cdot (S_{j'}^{\alpha}). \qquad (3)$$

In this way, the interface plane normal can be uniquely calculated. The habit planes between pearlitic ferrite and cementite in an annealed 0.81C-Fe alloy have been successfully determined with this method [8].
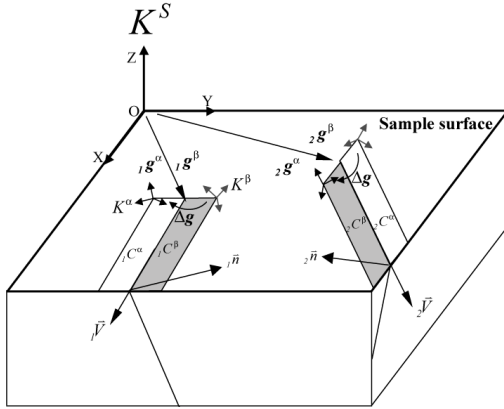
Fig. 1 Schematic drawing of interface traces from two pairs of phases that have the same kind of interface ${}_1\vec{V}$ and ${}_2\vec{V}$ are the interface trace vectors on the prepared sample surface. ${}_1\vec{n}$ and ${}_2\vec{n}$ are the interface plane normals
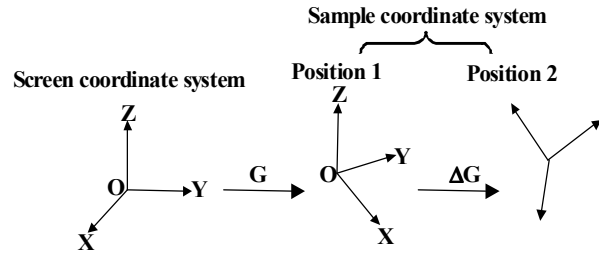
Fig. 2 Relative positions of the Screen coordinate system and the Sample coordinate system

Determination of surface crystallography of faceted nano-particles by TEM

The study of unconventional shaped nano-particles has recently become intensive due to their unique catalytic properties resulting from the high index surface facets. Naturally, the correct indexing of such surface planes constitutes one of the important bases for the further property and growth kinetics investigation. Therefore, a general and accurate determination method appears to be in need. In response to such a requirement, we developed a calculation method that can be applied to determine any faceted surface plane indices of nano-particles provided that the edges of the facets are visible and diffraction line patterns (Kikuchi) can be obtained under TEM imaging and diffraction mode.

The basic principle of this method is to determine the edge trace vectors that define the surface facets of a nano-particle in the TEM screen coordinate system and then obtain the surface plane normal by cross product and further calculate their Miller indices in the crystal coordinate system through coordinate transformation. The method is explained as follows.

For convenience, we introduce three Cartesian coordinate systems and one non-Cartesian coordinate system if the unit cell of the crystallite is not orthogonal. Of the three Cartesian coordinate systems, one is referenced to the screen of the TEM that records the image of the particle, with its Z-axis in the inverse direction of the incident electron beam, another coordinate system is set to the sample holder also with its Z axis in the inverse direction of the incident electron beam when the holder is in non-tilt position, and the third one to the crystal structure. If the Bravais lattice of the crystallite is not orthogonal, an additional non-Cartesian crystal coordinate system is convenient. Hereafter, we select the non-orthogonal Bravais lattice as the general case. The orientation relationships between the Cartesian coordinate systems are defined as a set of rotations transforming one system into the other, specified by three Euler angles in Bunge notation, see e.g. [9].

To determine the coordinates of a trace vector in the screen coordinate system, two sample positions are required. Assume that the unit trace vector in the sample coordinate system is $\boldsymbol{v}(x, y, z)$ and let the equivalent vectors in the screen coordinate system with respect to the two sample holder positions be $\boldsymbol{v}^1(x^1, y^1, z^1)$ (position 1) and $\boldsymbol{v}^2(x^2, y^2, z^2)$ (position 2). Under TEM imaging condition, let the orientation relationship between the screen coordinate system and the first sample position described by rotation $G(\varphi_1, \Phi, \varphi_2)$ and the rotation from the first sample position to the second sample position $\varDelta G(\Delta\varphi_1, \Delta\Phi, \Delta\varphi_2)$, as shown in Fig. 2. For the sake of simplicity, the first sample position could be taken without tilt operation. G is then characterized by a single rotation around the Z axis of the screen coordinate system caused by the electron beam, which is magnification dependent. Thus, the following relations between the unit vectors $\boldsymbol{v}$, $\boldsymbol{v}^1$ and $\boldsymbol{v}^2$ hold

$$\boldsymbol{v}^1 = M_1 \cdot \boldsymbol{v} \quad \text{and} \quad \boldsymbol{v}^2 = M_1 \cdot M_2 \cdot \boldsymbol{v}, \tag{4}$$

where M_1 and M_2 are the corresponding rotation matrices of G and $\varDelta G$, and are known. Then the relation between the $\boldsymbol{v}^1(x^1, y^1, z^1)$ and $\boldsymbol{v}^2(x^2, y^2, z^2)$ can be deduced as:

$$\boldsymbol{v}^1 = M_1 \cdot M_2^{-1} \cdot M_1^{-1} \cdot \boldsymbol{v}^2. \tag{5}$$

According to the imaging principle of the TEM system, an image of a nano-particle is the rotated (around the Z axis of the screen coordinate system and dependent on the magnification) and amplified projection of the particle. As the Z axis of the screen coordinate system is set parallel to the incident beam, *i.e.*, the Z axis is parallel to the projection direction, the X and Y coordinates of $\boldsymbol{v}^1$ and $\boldsymbol{v}^2$ in the screen coordinate system can be measured. Only z^1 and z^2 are unknown. With the linear equations offered by Eq. (2), the two unknown z^1 and z^2 can be resolved. Thus the coordinates of the trace vector in the screen coordinate system are determined.

The coordinate transformation from the screen coordinate system to the crystal coordinate system can be achieved through acquiring and indexing the electron diffraction pattern of the crystal. The coordinate transformation from the sample holder coordinate system to the Cartesian crystal coordinate system can be directly obtained by indexing the Kikuchi line pattern, e.g. with the software *Euclid Phantasies* (EP) [2, 3] and is expressed in three Euler angles $(\varphi_1, \Phi, \varphi_2)$ in Bunge notation. In such a way, the screen-to-reciprocal lattice base transformation matrix $M_{i \to r}$ and the screen-to-crystal coordinate system (not necessarily Cartesian) transformation matrix $M_{i \to nC}$ will be:

$$M_{i \to r} = M_i \cdot M_{EP} M_{C \to r} \quad \text{and} \quad M_{i \to nC} = M_i \cdot M_{EP} M_{C \to nC} \tag{6}$$

Notably, M_i is the rotation matrix from the screen to one of the sample holder positions where the Kikuchi pattern is acquired and M_{EP} is the transformation matrix from the sample holder coordinate system to the Cartesian crystal coordinate system, $M_{C \to r}$ is the matrix transforming from the Cartesian crystal coordinate system to the reciprocal lattice base and $M_{C \to nC}$ is the matrix from the Cartesian crystal coordinate system to the non-Cartesian crystal coordinate system. Therefore, for any vector obtained in the screen coordinate system $\boldsymbol{v}^i(x_i, y_i, z_i)$ that corresponds to the sample position acquiring the diffraction pattern, its Miller indices and the Miller indices of the plane normal to this vector can be obtained, respectively, as

$$\begin{bmatrix} u \\ v \\ w \end{bmatrix} = M_{i \to nC}^{-1} \cdot \begin{bmatrix} x_i \\ y_i \\ z_i \end{bmatrix} \text{ and } \begin{bmatrix} h \\ k \\ l \end{bmatrix} = M_{i \to r}^{-1} \cdot \begin{bmatrix} x_i \\ y_i \\ z_i \end{bmatrix}. \tag{7}$$

In this way, the crystalline directions of the edges and the surface planes of a nano-particle can be determined. This method has been successfully applied to determine the surface plane and edge vector indices of hematite particles enclosed by high index planes [5].

Determination of twinning elements

Twinning is a frequent physical process occurring either during mechanical deformation or during phase transformation. Determination of the twin type and twinning elements appears important as this offers useful information to understand the physical process of twinning and therefore has long been a topic in the domain of materials science. Previously, twin type and twinning elements were mainly determined by TEM. It requires specific sample on-edge positions to ambiguously decide the twinning type; therefore the determination process is complicated and not straightforward. Based on the misorientation calculation using the EBSD (SEM) individual orientation data, we proposed a calculation method to simplify this process, as described below.

The misorientation between two crystals is defined by sets of rotations from one of the symmetrically equivalent coordinate systems of one crystal to another equivalent coordinate system of the other crystal. The measured orientation g of a crystal characterized by three Euler angles (φ_1, Φ, φ_2) (Bunge notation, see e.g. [9]) with respect to the macroscopic sample reference can be described by a rotation matrix that transforms the sample coordinate system into the Cartesian crystal coordinate system. Owing to the crystal symmetry, g has certain equivalents, expressed by $S_i g$, where S_i is the generic element of rotation symmetry group. The misorientation between the matrix and its twinned crystal can be expressed by Δg:

$$\Delta g \ S_j g_T = S_i g_M, \ or \ \Delta g = S_i g_M \ g_T^{-1} \ S_i^{-1}. \tag{8}$$

If we denote $\Delta g = \begin{pmatrix} a_{11} & a_{12} & a_{13} \\ a_{21} & a_{22} & a_{23} \\ a_{31} & a_{32} & a_{33} \end{pmatrix}$

then the misorientation angle ω and rotation axis $\mathbf{d}$ can be derived as:

$$\cos \omega = \frac{a_{11} + a_{22} + a_{33} - 1}{2} \tag{9}$$

$$\mathbf{d} = (d_1, d_2, d_3) = \left(\frac{a_{23} - a_{32}}{2 \sin \omega}, \frac{a_{31} - a_{13}}{2 \sin \omega}, \frac{a_{12} - a_{21}}{2 \sin \omega} \right) \text{ (if } \omega \neq 180°) \tag{10}$$

$$\mathbf{d} = \begin{matrix} \pm \sqrt{(a_{11} + 1)/2} \\ \pm \sqrt{(a_{22} + 1)/2} \\ \pm \sqrt{(a_{33} + 1)/2} \end{matrix} \text{ with } \begin{matrix} d_m = max(|d_i|, \ i = 1,2,3) \\ d_m > 0 \ \text{(by convention)} \\ \forall i \neq m, \ sgn(d_i) = sgn(a_{im}) \end{matrix} \text{ (if } \omega = 180°), \tag{11}$$

where d_1, d_2 and d_3 are the coordinates of the rotation axis in the Cartesian crystal coordinate system and sgn stands for sign function. According to the definition of twin orientation relationship, there exists at least one 180° rotation. If the Miller indices of the plane normal to the rotation axis are rational, the twinning mode belongs to type I and K_1 is determined. If the Miller indices of the

rotation axis are rational, the twinning mode belongs to type II and η_1 is determined. According to the minimum shear criterion and the Bilby–Crocker theory [10], the complete twinning elements (K_1 – the twinning plane; η_1 – the twinning direction; K_2 – the reciprocal or conjugate twinning plane; η_2 – the reciprocal or conjugate twinning direction; P – the plane of shear; s – the amount of shear) of two types of twins can be calculated.

Summary

Methods to determine some specific crystallographic elements of interface plane, surface plane of nano-particles and twin type and twinning elements based on the orientation data acquired through SEM (EBSD) or TEM have been summarized in the present work. The methods are useful for the related studies.

Acknowledgements

References

[1] F. J. Humphreys: J. Mater. Sci. Vol. 36 (2001), p. 3833

[2] A. Morawiec: J. Appl. Cryst. Vol. 32 (1999), p. 788

[3] A. Morawiec, J.-J. Fundenberger, E. Bouzy and J.-S. Lecomte: J. Appl. Cryst. Vol. 35 (2002), p. 287

[4] Y. D. Zhang, C. Esling, X. Zhao and L. Zuo: J. Appl. Cryst. Vol. 40 (2007), p. 436

[5] S. Li, Y. Zhang, C. Esling, J. Muller, J.-S. Lecomte, G. Qin, X. Zhao and L. Zuo: J. Appl. Cryst. Vol. 42 (2009), p. 519

[6] D. Y. Cong, Y. D. Zhang, Y. D. Wang, C. Esling, X. Zhao and L. Zuo: J. Appl. Cryst. Vol. 39 (2006), p.723

[7] C. S. Barrett: *Structure of Metals*. 2nd ed. (New York: McGraw Hill Book Co., 1952).

[8] Y. D. Zhang, C. Esling, M. Calcagnotto, X. Zhao and L. Zuo: J. Appl. Cryst. Vol. 40 (2007), p. 849

[9] H. J. Bunge, C. Esling and J. Muller: J. Appl. Cryst. Vol. 13 (1980), p. 544

[10] B. A. Bilby and A. G. Crocker: Proc. R. Soc. Ser. A Vol. 288 (1965), p. 240

Two- and Three-Dimensional EBSD Measurement of Dislocation Density in Deformed Structures

David P. Field[a], Colin C. Merriman[b] and Ioannis N. Mastorakos[c]

School of Mechanical and Materials Engineering, Washington State University,
Pullman, WA 99164-2920, USA

[a]dfield@wsu.edu, [b]merrimac@wsu.edu, [c]mastorakos@wsu.edu

Abstract. Electron backscatter diffraction (EBSD) techniques have been used to measure the dislocation density tensor for various materials. Orientation data are typically obtained over a planar array of measurement positions and the minimum dislocation content required to produce the observed lattice curvature is calculated as the geometrically necessary (or excess) dislocation density. The present work shows a comparison of measurements in two-dimensions and three-dimensions using a dual beam instrument (focused ion beam, electron beam) to obtain the data. The two-dimensional estimate is obviously lower than that obtained from three-dimensional data since the 2D analysis necessarily assumes that the third dimension has no curvature in the lattice. Effects of the free-surface on EBSD measurements are discussed in conjunction with comparisons against X-ray microdiffraction experiments and a discrete dislocation dynamics model. It is observed that the EBSD measurements are sensitive to free-surface effects that may yield dislocation density observations that are not consistent with that of the bulk material.

Introduction

Plastic deformation in crystalline materials is facilitated by dislocation motion that acts on specific slip systems under given loading conditions. The early work of Schmid and others has laid the foundation for a rich body of research in this area of investigation. Schmid's law predicts that slip will occur in a single crystal on the slip system subjected to the highest resolved shear stress. Many authors have noted conditions for non-Schmid behavior in various materials under given conditions. A new experimental technique for deformation of oriented single crystal materials (termed the six degree of freedom) offered one such observation of non-Schmid slip behavior [1].

During plastic deformation of crystalline materials, so-called geometrically necessary dislocations (or excess dislocations) accommodate orientation gradients within single crystallites in the material. This dislocation structure is necessary to maintain lattice continuity. The concept of geometrically necessary dislocations was first introduced by Nye [2].

Nye's dislocation density tensor α_{ij} quantifies the content of dislocations in the lattice with Burgers vector i and the dislocation line vector j. Any dislocation structure that makes no contribution to the dislocation density tensor, such as a dislocation dipole, is termed statistically stored dislocations. Assuming a minimal effect from elastic strain gradients, any crystallite containing non-zero dislocation density tensor components necessarily contains lattice curvature that can be quantified by spatially specific orientation measurements. Such measurements are inherent to automated EBSD scans of crystalline materials. A detailed description of the geometrically necessary dislocation is given by Arsenlis and Park [3]. It is possible to relate the dislocation density tensor, α, to the dislocations present in the neighborhood by the relation:

$$\alpha = \sum_{i=1}^{K} \rho^i (b^i \otimes z^i) \tag{1}$$

where, the dislocation dyadic represents a geometrical definition of dislocation i having Burgers vector b^i and slip plane normal direction z^i. The sum is over all the dislocations present and ρ^i is the scalar dislocation density of dislocation i. Since the dislocation density tensor has 9 components it is possible, using a linear simplex method, to determine a set of densities of 9 dislocation types which minimizes the total dislocation content. One disadvantage of using this technique is that it does not take into account all the types of dislocations that could contribute to lattice curvature. This limitation could be overcome by using a normal equation lower bound method (as shown by El-Dasher et al [4]) where equation (1) for FCC materials could be reduced to:

$$\alpha_l = A_{lk}\rho_k, \; k = 1, 36 \text{ and } l = 1, 9 \tag{2}$$

where the matrix A represents a component of the dislocation dyadic. Using the L^2 minimization method it is possible to compute the densities of all 36 dislocations, where equation (3) reduces to

$$\rho_{GN} = A^T(AA^T)^{-1}\alpha \tag{3}$$

In the current analysis we have limited the dislocation types to pure edge and pure screw and hence code was developed to determine the densities of 18 total dislocation types (12 pure edge and 6 pure screw dislocations). To determine an accurate estimate of GND density when analyzing poly-crystalline materials, it is necessary to ignore the high angle grain boundaries from the calculation of GND. In the current analysis this is generally not necessary since measurements are made on lightly deformed single crystals. Nevertheless, the code ignores positions wherever the point-to-point misorientation exceeds 10°.

Experimental Details

One sample of polycrystalline AA 7050 T7451 was deformed and characterized using EBSD. No further heat treatment was conducted leaving the material in the as received condition. The sample was deformed at room temperature using channel die compression to a 5% height reduction at a strain rate of ~ 5.5×10^{-3} s^{-1} to simulate cold rolling of aluminum. Four serial sections were produced using a dual beam instrument (focused ion beam (FIB)/SEM) for sectioning and analysis. The data analysis was performed using in house software that includes the calculation of the dislocation density tensor and the ability to perform this calculation across multiple datasets.

The 4 plane serial section data set from the channel die deformed AA 7050 specimen contained ~244,000 points and a volume of 2500 μm^3, the step size used for these datasets was 0.25 μm with each FIB milling process removing 0.25 μm of material.

In a second experiment, single crystal copper, 99.99% pure and with the <2 9 20> direction aligned with the deformation axis, was deformed 10 percent in uniaxial compression using a six-degrees of freedom testing apparatus [1]. The orientation was selected so that a {111}<110> type slip system would lie exactly in coincidence with the direction of maximum resolved shear stress. EBSD scans were performed using step sizes ranging from 0.1 μm to 100 μm on a polished surface taken from the interior of the specimen. All scans were made near the central part of the prepared surface so as to avoid any edge or surface effects with the compression direction vertical on the images. A similar set of measurements was performed on a mating surface of this specimen using x-ray microdiffraction [5]. A complete description of the experiment and the characterization performed is found in reference [6]. Staker and Holt used TEM imaging techniques to measure the dislocation density in a Cu specimen deformed 10 percent in tension to be 118×10^{12} m^{-2} [5]. Similar results were obtained by Heuser using neutron scattering techniques who measured 1.9×10^{14} m^{-2} at 16% compression of Cu single crystals [6]. The excess dislocation content was determined from the data obtained from the plane sections using the assumption that there is no lattice curvature in the through-thickness direction.

Results

2D and 3D EBSD. Figure 1 shows an orientation image of the 2nd serial section of the sample (the orientation color key for orientations normal to the plane of the specimen surface is included for reference). Figure 2 shows the 2-D and 3-D excess dislocation density maps generated from the same data represented in the orientation image shown in Figure 1. White areas are regions of high excess dislocation density while black regions are grain boundaries or low confidence data. The gray scale indicates black for regions of excess dislocation density less than 10^{11} m^{-2} to white for densities of 10^{15} m^{-2} on a linear scale. Table 1 shows all pertinent data calculated for the 2-D and 3-D excess dislocation density. Dislocation densities are not determined for the first and fourth slices of the 3-D dataset because these are the edges of the 3D volume analyzed and the software requires that data be present on all sides of the position being analyzed. The gray scale indicates black for regions of excess dislocation density less than 10^{11} m^{-2} to white for densities of 10^{15} m^{-2}.

Analysis on similar specimens but with a far larger number of section planes has yielded similar results. The three-dimensional dislocation density is a factor of two higher than the estimates obtained from data on plane sections. The obvious question of the researcher relates to the reliability of the plane section data in relation to the bulk material since EBSD involves measurement on a free surface.

Table 1 – Excess Dislocation Density (EDD) after 5% Deformation in AA 7050

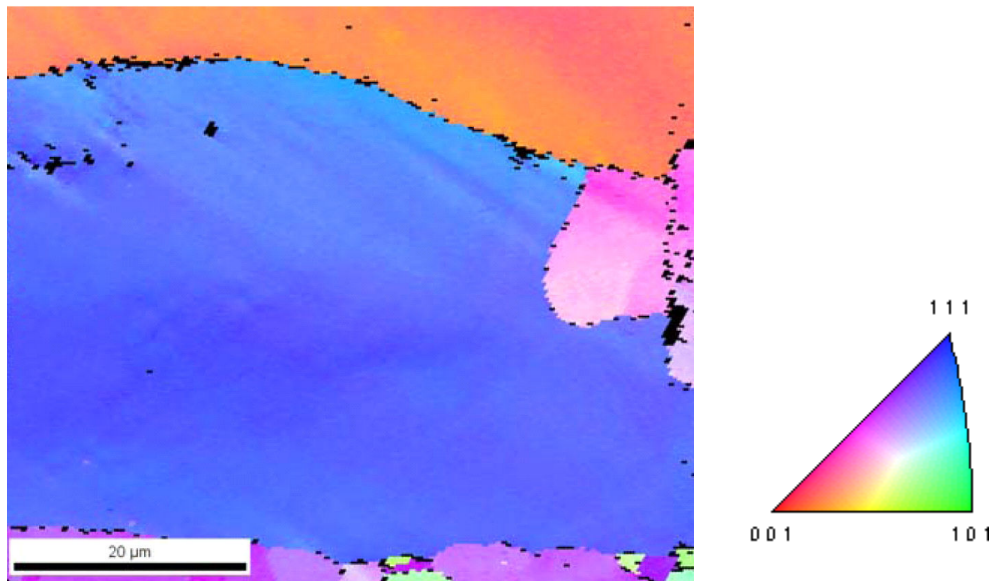| Serial Section	2-D EDD [10^{12} m^{-2}]	3-D EDD [10^{12} m^{-2}]
1	922	--
2	958	1851
3	942	1722
4	965	--
Numerical Average	946	1786

Figure 1 – Orientation image of serial section 2 (with the corresponding orientation shading key) for AA 7050 T7541 deformed in channel die compression to a 5% height reduction at a strain rate of ~ 5.5 x 10^{-3} s^{-1}. The average excess dislocation density was 1786 x 10^{12} m^{-2} as determined from the 3-D data and 946 x 10^{12} m^{-2} as measured from the 2-D sections.

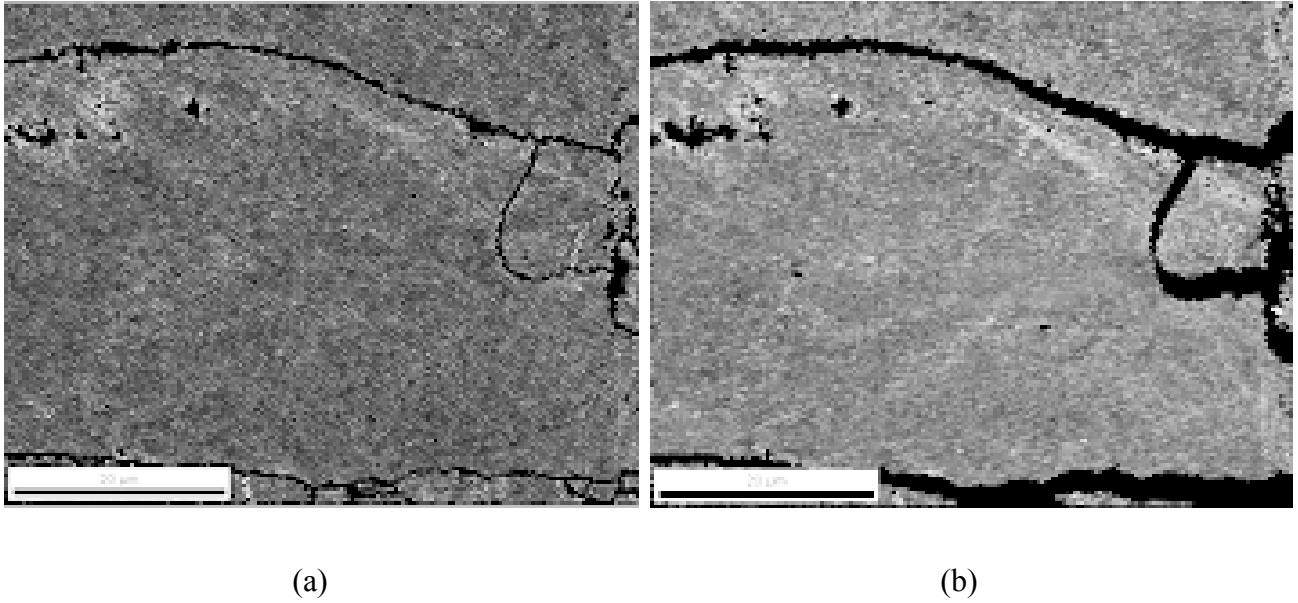<div align="center">(a)   (b)</div>

Figure 2 – (a) 2-D and (b) 3-D excess dislocation density maps for serial section 2. The 2-D excess dislocation density was 958 x 10^{12} m^{-2} and the 3-D excess dislocation density was 1851 x 10^{12} m^{-2}. The shading scale goes from black = 10^{11} m^{-2} to white = 10^{15} m^{-2}.

EBSD and x-ray micro-diffraction (XRM). The pure copper single crystals deformed using the six-degree-of-freedom testing apparatus were sectioned through the specimen center such that the slip plane normal and the slip direction were both contained in the section plane. Each side of the specimen was polished and one was used for EBSD analysis while the other was analyzed using XRM. The misorientation distribution was similar using both techniques with the misorientations ranging from 0 to 5° off the nominal orientation of the crystal. The primary difference in the measurements was in the sharpness of the images. The EBSD data indicated a loose wall of dislocation tangles as evidenced by the slowly changing orientation of the crystal lattice through the subcell structure. The XRM data, on the other hand, showed a sharp change in orientation at the subcell boundaries. Figure 3 shows point-to-point misorientations for both the XRM and EBSD analyzed regions, where the maximum misorientation is about 0.3°. The difference in these results is attributed to the free surface effects which likely allowed the dislocation structure to relax in the near surface region (where the EBSD data are obtained ~10 nm below the free surface), while the dislocation structure was more well-defined in the bulk of the material. This bulk region is where the XRM data are obtained (on the order of a few microns below the specimen surface). Dislocation dynamics calculations were employed to investigate the extent of the near-surface dislocation structure relaxation and to determine if this could indeed be used to explain the difference in the observed data.

Dislocation Dynamics Calculations. In dislocation dynamics, each dislocation is represented as a curved line. The simulated three-dimensional space is usually a cube with edge dimensions varying from 3 to 30 μm, representing a single crystal. The dislocation lines are approximated with sets of discrete straight-line segments. This geometry allows calculation of the overall self - stress of the curved dislocation lines using the sum of the self - stresses of all the line segments which is known from the literature [9]. Then, the interaction between dislocation segments can be calculated using the expression for the Peach-Koehler force:

$$\mathbf{F}_i = \sigma_i^{\text{total}} \cdot \mathbf{b}_i \times \xi_i + \mathbf{F}_{i-\text{self}}$$

(4)

where $\mathbf{b}_i$ represents the Burger vector and ξ_i the line sense of a dislocation segment i. The last term $\mathbf{F}_{i-self}$ is the force due to the local interaction between the segment adjustment to nodes j and $j+1$. The

total stress tensor σ_i^{total} at a given point is the sum of stresses from all dislocations, defects, cracks or any other internal and external agencies.

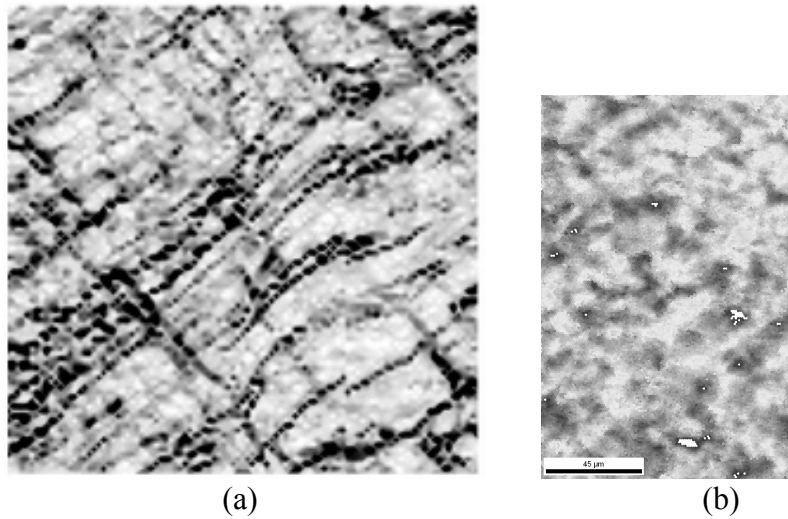(a)   (b)

Figure 3 – Point to point misorientations shown for (a) XRM data and (b) EBSD data. The micron bar shown in the EBSD image is 45 µm and is the same scale for the XRM and EBSD based images.

The point where two discrete dislocation segments meet is a node. Each node has in general three degrees of freedom unless is restricted for special reasons (e.g. surface nodes, pined nodes, etc.). A typical dislocation dynamics configuration can include thousands of nodes. During the simulation, all nodes move simultaneously in the glide direction over a characteristic time corresponding to the time increment required for an interaction to take place. The result is a set of nonlinear differential equations governing the motion of the dislocation segments. The governing equation of glide motion for each dislocation node is a modification of Newton's second law:

$$m_i^* \frac{d\mathbf{v}_i}{dt} + \frac{1}{M_i(T,p)} \mathbf{v}_i = \mathbf{F}_i^{glide-component}$$

(5)

where m_i^* is the effective mass per unit dislocation, M is the mobility which depends on both temperature T and pressure p, $\mathbf{v}_i$ is the glide velocity of segment i and $\mathbf{F}_i$ is the glide component of the Peach-Koehler force [10].

In our case, parallel dislocations of mixed character were inserted into a simulation box representing a single crystal. The orientation of the specimen was <100>, <010> and <001> along x, y and z axes respectively. A "free" surface was then created by introducing image forces in the simulation box at an orientation normal to the dislocation lines. The structure was allowed to relax from this configuration by running the model for a certain amount of time without any external applied load. The images forces and interaction forces between the dislocations caused the dislocations to move towards the free surface. The parts of the dislocation lines nearest the free surface repelled one another and were in a significantly distorted arrangement to a depth of about 300 Burger's vector (which corresponds to a distance of approximately 65 nm below the free surface. Figure 4.a shows a view of a 3D structure consisting of straight dislocation walls that intersect a free surface with the minimum possible dislocation line length. As the structure relaxes by dislocation interactions and image forces at the free surface, the structure coarsens near the surface but remains compact in the bulk of the material (Fig. 4.b). This is the range from whence the EBSD signal originates. The XRD measurement occurs significantly deeper in the "bulk" of the material (at least a few microns into the specimen), where the dislocations were still in a tight wall configuration in our simulation.
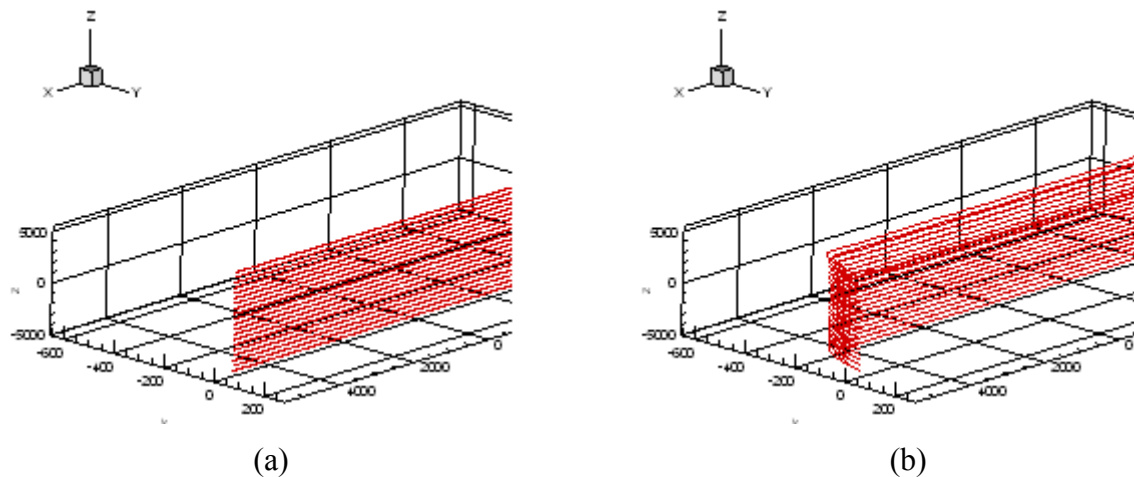
<center>(a)   (b)</center>

Figure 4 – Dislocation dynamics simulations showing the initial dislocation wall, and the spread in the dislocation structure near the free surface after allowing for relaxation of the structure.

Summary

A comparison of excess dislocation density measurements using 2D and 3D EBSD scans were performed. Results indicated that the trend was similar for these measurements, and on the same order of magnitude as results reported in literature. Estimates of dislocation densities from the 3D data were approximately a factor of two greater than those obtained from the 2D sections. Depending on the character of the dislocation structure with respect to the section plane, these results may vary.

The EBSD vs. XRM analysis showed that the surface sensitivity of the EBSD measurements can affect the character of the observed dislocation structures. The relatively small deformation for which the observations were made resulted in dislocation structures that were not well developed, and subsequently relaxed near the specimen surface. The XRM technique showed the true character of the bulk dislocation structure while the EBSD measurements were negatively influenced by the free surface on which the measurements were made.

References

[1]   J.N. Florando, M.M. LeBlanc and D.H. Lassila: Scripta Mater. Vol. 57 (2007), p. 537

[2]   J.F. Nye: Acta Met. Vol. 1 (1953), p. 153

[3]   A. Arsenlis and D.M. Parks: Acta Mater. Vol. 47 (1999), p. 1597

[4]   B.S. El-Dasher, B.L. Adams and A.D. Rollett: Scripta Mater. Vol. 48 (2003), 141

[5]   K.R. Magid, J.N. Florando, D.H. Lassila, M.M. LeBlanc, N. Tamura and J.W. Morris, Jr.: Phil. Mag. Vol. 89 (2009), p. 77

[6]   D.P. Field, K.R. Magid, I.N. Mastorakos, J.N. Florando, D.H. Lassila, and J.W. Morris, Jr.: Phil. Mag.   *In Press*.

[7]   M.R. Staker and D.L. Holt: Acta Metall. Vol. 20 (1972), p. 569

[8]   B.J. Heuser: J. Appl. Cryst. Vol. 27 (1994), p. 1020

[9]   J.P. Hirth and J. Lothe: *Theory of Dislocations*. Krieger Publ. Company, Malabar, (1982)

[10] H.M. Zbib and T. Diaz de la Rubia: Int. J. Plasticity Vol. 18 (2002), p. 1133.

Texture Control in Non-Oriented Electrical Steels by Severe Plastic Deformation

L.A.I. Kestens[1,a], R. Petrov[1,b], P. Gobernado[2,c] and E. Leunis[3,d]

[1] Ghent University, Materials Science and Engineering, Technologiepark 903, Gent, Belgium

[2] Delft University of Technology, Materials Science and Engineering, Mekelweg 2,
NL-2628 Delft, The Netherlands

[3] ArcelorMittal Research Industry Ghent, OCAS N.V, Kennedylaan 3, Zelzate, Belgium

[a] Leo.Kestens@ugent.be, [b] roumen.petrov@ugent.be, [c] p.gobernadohernandez@tudelft.nl,
[d] elke.leunis@arcelormittal.com

Abstract. Although plenty of research has already been carried out on the issue of texture control in non-oriented electrical steels, there is not yet a universally applied industrial process to obtain an optimized {001} fibre texture. Among the various laboratory processes that have been studied so far, cross rolling seems to be one of the most promising approaches. For evident reasons cross-rolling cannot be implemented on a conventional continuous rolling line of an industrial plant. In the present study a potential interesting alternative is presented which may deliver a similar texture evolution as the cross rolling process, but can be applied in a continuous line of hot and cold rolling operations followed by recrystallization annealing. By applying severe rolling reductions a very strong rotated cube texture is obtained very much similar to the one that is observed after cross rolling. After annealing, the rotated cube texture changes to a {h11}<1/h,21> fibre texture with a maximum on the {311}<136> component which implies the potential to develop a {001} fibre texture after further processing. It is argued that the appearance of the {311}<136> recrystallization texture component can be attributed to oriented nucleation in the vicinity of grain boundaries between slightly misoriented rotated cube grains.

Introduction

In the technical literature two grades of electrical steels are distinguished. Grain oriented (GO) electrical steels are employed as magnetic flux carriers in power transformer devices. They are characterized by a very strong Goss texture ({110}<001>) for which the <001> crystal directions are aligned with the direction of external magnetization. Conversely, non-oriented (NO) electrical steels are applied to carry magnetic flux in rotating electro-magnetic devices such as electrical motors. For NO electrical steels the optimum texture is the {001} or θ-fibre texture, which maximizes the density of <100> spontaneous magnetization directions along the flux lines of the rotating applied field. GO and NO electrical steels are facing the scientific and technical community with an opposing paradigm. Whereas the technical problem of manufacturing GO electrical steels has been solved long ago by virtue of the Goss patent [1], there still remains a lively scientific debate on the origin of the Goss texture during secondary recrystallization [e.g. 2, 3]. For NO electrical steels, however, a solid body of scientific knowledge on orientation selection has not yet produced a single standard manufacturing method that is applied worldwide.

Although a large body of literature [e.g. 4, 5, 6] has already been published on texture control in NO electrical steels, most methods have only proven to be successful in the laboratory and are difficult to be implemented on an industrial manufacturing line. Moreover, the boundary conditions of GO and NO steel manufacturing are very different. GO steels are products of high added value
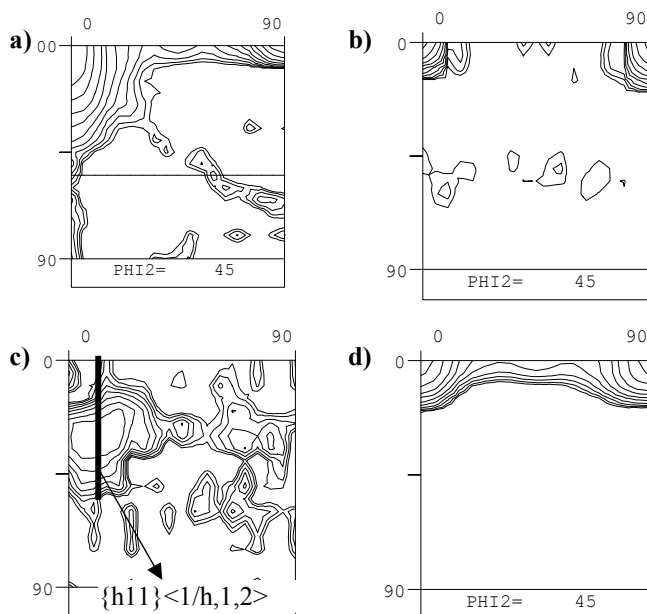
Figure 1. ODFs observed after cross rolling: hot band texture (a), cold rolled texture (b), primary recrystallized (c) and after an additional annealing treatment (d).

and relatively low production volumes, which justify the investment of dedicated production lines that are nearly exclusively used for GO production. NO electrical steels, however, are of lower added value but are produced in larger quantities on conventional low-carbon sheet production lines. This imposes more stringent boundary conditions on the production of NO steels.

Kestens and Jacobs [7] have published a review in which it was claimed that the magnetic quality of the texture can hardly be affected by varying a broad variety of process parameters within the limits of a conventional integrated steel making, hot and cold rolling plant. This was illustrated by monitoring the evolution of the A-parameter[†], which was employed to quantify the magnetic quality of the texture.

The A-parameter value may theoretically vary between the limits of 0 and 54.7° for single crystals with the <100> and <111> directions parallel to the magnetization direction, respectively. By modifying the chemical composition in addition to a wide variety of process parameters (such as the slab reheating temperature, the finish rolling temperature, the coiling temperature, the cold rolling reduction, the recrystallization time or temperature and the skin pass reduction) the A-values only varied between 25 and 31°; the latter A-value corresponding to the value of a random textured material. Hence, it was concluded that additional, non-conventional measures of texture control are required to obtain better results.

One potential strategy reported by Kestens and Jacobs [7] is cross-rolling. By hot rolling a NO electrical steel with 0.5 to 1% Si and ~0.02%C in the two-phase austenite/ferrite region a hot band texture is obtained with a strong α-fibre (<110>//RD) and an intense maximum of ~30 x on the rotated cube component (cf. Fig. 1a). When the sheet is 90° rotated after hot rolling and thus, the direction of cold rolling is perpendicular to the direction of hot rolling, the ensuing cold rolling texture exhibits an extremely intense maximum of ~150 x on the rotated cube component ({001}<110>), cf. Fig. 1b. After primary recrystallization at the conventional temperatures of 750 to 850 °C of a current practice continuous annealing line, a relatively weak texture is obtained with a maximum of <5 x on the {311}<136> component which is positioned on the {h11}<1/h,12> fibre reported by Homma et al. [8] and Gobernado et al. [9], cf. Fig. 1c. In itself this texture does not exhibit an interesting magnetic quality, but when the annealed material is further cold rolled to a reduction of 4 to 8%, followed by another annealing treatment, a very different texture arises with a strong maximum of ~50 x on the rotated cube component and some intensity distribution over the entire θ-fibre, cf. Fig. 1d. The exceptional magnetic quality of the ODF of Fig. 1d is reflected in the very low direction-averaged A-value of 24.3°. It is obvious, though, that cross rolling cannot be implemented in a line manufacturing process.

[†] The A-parameter is the weighted average of the angles between one arbitrary magnetization direction and the closest <100> crystal direction of the orientations that are present in the ODF f(g). The direction averaged A-parameter is the average A-parameter for an applied magnetic field in three different directions: RD, TD and 45° to RD. The theoretical minimum value of the direction averaged A-parameter is 22.5°.

Accumulative Roll Bonding

In an attempt to investigate the grain refining effect of severe rolling reductions, an IF-steel was cold rolled to various reductions, following the accumulative roll bonding (ARB) process proposed by Tsuji et al. [10]. After 10 ARB passes at room temperature, an accumulated rolling strain is obtained of 6.93 (true logarithmic strain) which corresponds to an accumulated reduction of 99.9%. The ensuing rolling texture exhibits a strong α-fibre with an intense maximum of ~30x on the rotated cube component, cf. Fig. 2a. Upon annealing of such an excessively cold rolled material a recrystallization texture appears which is very much similar to the one observed after cross-rolling of the NO electrical steel, i.e. with a maximum in the vicinity of {311}<136> component on the {h11}<1/h,12> fibre as shown in Fig. 2b (compare with Fig. 1c).

Figure 2. ARB textures corresponding to a cumulated reduction of 99.9%: deformed texture (a) and annealed texture (b), and to a cumulated reduction of 99.6%: deformed texture (c) and annealed (d) texture.

A similar trend was observed even after a somewhat less severe cold rolling, i.e. after the 8th ARB pass yielding a true strain of 5.55 which corresponds to an accumulated reduction of 99.6%. Fig. 2c illustrates that a strong rotated cube component is present in the rolling texture, even though the absolute ODF maximum is on the {332}<110> component. After annealing, however, an equally strong {311}<136> recrystallization component is present, cf. Fig. 2d. These observations made us conjecture that the successful trail of NO steel texture control by cross rolling could be mimicked by applying excessive rolling strains whilst omitting rotating the sheet 90° between hot and cold rolling. This would render the procedure far friendlier to an industrial process of line production.
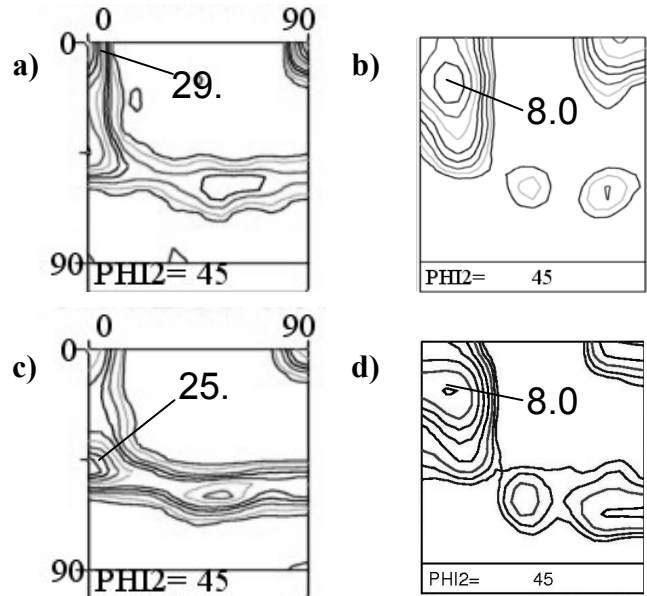
Severe Plastic Deformation of NO Electrical Steel

The concept of severe plastic deformation was applied on a NO steel grade with more than 2% Si and hence a single ferrite structure over the entire solid domain. In order to avoid excessive cold rolling reductions, which cannot be applied in an industrial installation, it was decided to carry out hot rolling below the Tnr temperature (recrystallization stop temperature), so as to accumulate the reductions of hot and cold rolling. The processing schedule is schematically represented in Fig. 3.
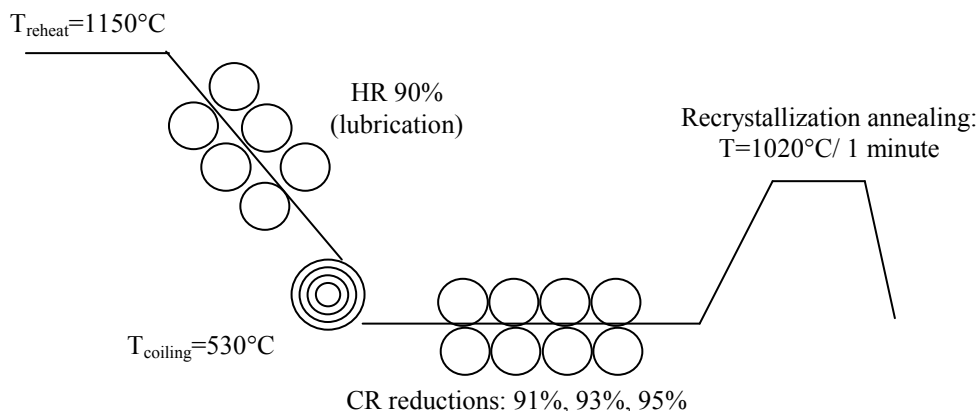

Figure 3. Representation of the thermo-mechanical schedule applied during severe plastic deformation.